

# Predicting calvarial growth in normal and craniosynostotic mice using a computational approach

Arsalan Marghoub<sup>1</sup>, Joseph Libby<sup>2</sup>, Christian Babbs<sup>3</sup>, Erwin Pauws<sup>4</sup>, Michael J Fagan<sup>2</sup>, Mehran Moazen<sup>1</sup>

<sup>1</sup>Department of Mechanical Engineering, University College London, Torrington Place, London, WC1E 7JE, UK

<sup>2</sup>Medical and Biological Engineering, School of Engineering and Computer Science, University of Hull, Hull, HU6 7RX, UK

<sup>3</sup>Weatherall Institute of Molecular Medicine, University of Oxford, Oxford, OX3 9DS, UK

<sup>4</sup>Great Ormond Street Institute of Child Health, University College London, Guilford St, London, WC1N 1EH, UK

*Corresponding author:*

*Mehran Moazen; Department of Mechanical Engineering, University College London, Torrington Place, London, WC1E 7JE, UK; T:+44 (0) 207 679 3862; E: M.Moazen@ucl.ac.uk*

## Abstract

During postnatal calvarial growth the brain grows gradually and the overlying bones and sutures accommodate that growth until the later juvenile stages. The whole process is coordinated through a complex series of biological, chemical and perhaps mechanical signals between various elements of the craniofacial system. The aim of this study was to investigate to what extent a computational model can accurately predict the calvarial growth in wild type (WT) and mutant type (MT) *Fgfr2*<sup>C342Y/+</sup> mice displaying bicoronal suture fusion. A series of morphological studies were carried out to quantify the calvarial growth at P3, P10 and P20 in both mouse types. Then, microCT images of a P3 specimen were used to develop a finite element model of skull growth to predict the calvarial shape of WT and MT mice at P10. Sensitivity tests were performed and the results compared to *ex vivo* P10 data. While the models were sensitive to the choice of input parameters, they predicted the overall skull growth in the WT and MT mice. The models also captured the difference between the *ex vivo* WT and MT mice. This modelling approach has the potential to be translated to human skull growth and enhance our understanding of the different reconstruction methods used to clinically manage the different forms of craniosynostosis, and in the long term possibly reduce the number of re-operations in children displaying this condition and thereby enhance their quality of life.

**Keywords:** biomechanics; development; calvarial bones; sutures; finite element method

**Running title:** Modelling calvarial growth

This is the peer reviewed version of the following article: Marghoub, A., Libby, J., Babbs, C., Pauws, E., Fagan, M. J. and Moazen, M. (2017), Predicting calvarial growth in normal and craniosynostotic mice using a computational approach. *J. Anat.* doi:10.1111/joa.12764 which has been published in final form at <http://onlinelibrary.wiley.com/doi/10.1111/joa.12764/abstract>. This article may be used for non-commercial purposes in accordance with Wiley Terms and Conditions for Self-Archiving.

## 45 1- Introduction

46 The mammalian cranial vault principally consists of five flat bones joined along their edges  
47 by soft tissues termed sutures (Opperman, 2000; Morriss-Kay & Wilkie 2005; Herring, 2008).  
48 The sutures are where most of the skull vault growth occurs and they also function to give  
49 the bones flexibility for birth and to allow the skull to expand and grow as the brain enlarges  
50 (Cohen, 2005; Richtsmeier & Flaherty, 2013). Premature closure of the sutures, or  
51 craniosynostosis, is a medical condition that occurs in about 1 in 2500 births, the question of  
52 an occurrence rate increase has also been raised (Boulet et al. 2008; van der Meulen et al.  
53 2009; Johnson & Wilkie, 2011; Cornelissen et al. 2016). The majority of cases (70%) are  
54 non-syndromic i.e. single suture synostosis, with the remaining instances being syndromic  
55 (e.g. Crouzon and Apert), in which more than one suture fuses and where additional features  
56 are present such as midfacial hypoplasia (Morriss-Kay & Wilkie, 2005). Children displaying  
57 craniosynostosis generally require a surgical procedure that in majority of cases is carried  
58 out at 6-12 months of age.

59 Research to understand the genetic basis and clinical course of craniosynostosis (Wilkie,  
60 1997; Morriss-Kay & Wilkie, 2005; Al-Rekabi et al. in press) has led to the development of  
61 various animal models (Mooney et al. 1998; Grova et al. 2012; Holmes, 2012). Mice have  
62 been investigated extensively in this work because murine calvarial morphology and  
63 genetics share several similarities with humans with the advantage that the developmental  
64 process occurs over a much shorter period (Morriss-Kay & Wilkie, 2005). In terms of  
65 calvarial development the intracranial volume of wild type mice typically reaches 70% of the  
66 adult size by postnatal day 10 (P10) with minimal further growth after P20 (Aggarwal et al.  
67 2009; Moazen et al. 2016). In contrast, human intracranial volume reaches 65% of the adult  
68 volume by 1 year, with minimal further growth after 10 years (Dekaban, 1977; Sperber,  
69 1989).

70 The Crouzon mouse model ( $Fgfr2^{C342Y/+}$ ) has been extensively studied and has become a  
71 well-established model for investigating craniosynostosis (Eswarakumar et al. 2004; Perlyn  
72 et al. 2006; Liu et al. 2013; Martinez-Abadias et al. 2013; Peskett et al. 2017). This line is  
73 particularly interesting since it exhibits robust phenotypic abnormalities with features  
74 recapitulating clinical abnormalities observed in patients. The coronal sutures (joining the  
75 parietal and frontal bones) are primarily affected in these mice as well as other joints on the  
76 cranial base (e.g. intersphenoidal synchondrosis suture joining presphenoid and  
77 basisphenoid bones), causing a predictable brachycephalic (wide and short) head shape also  
78 characteristic of Crouzon patients (Eswarakumar et al. 2004; Perlyn et al. 2006; Liu et al.  
79 2013). Coronal sutures in the wild type mouse appear to be closed (while never fully fused)  
80 at postnatal day thirty (P30), while in the Crouzon mouse overlapping of the frontal and  
81 parietal bones at this suture begins at the embryonic stages (E18.5) with full closure  
82 occurring at ~P20 (Eswarakumar et al. 2004; Perlyn et al. 2006). Thus, Crouzon  $Fgfr2^{C342Y/+}$   
83 mutant type (MT) and wild type (WT) mice provide an invaluable tool with which to  
84 understand the biomechanics of craniosynostotic and normal skull growth during postnatal  
85 development.

86  
87 The finite element (FE) method is a computational modelling technique that has been widely  
88 used to understand general craniofacial biomechanics (e.g. Ross et al. 2005; Rayfield, 2007;  
89 Curtis et al. 2011; Cox et al. 2012; Moazen et al. 2013; Gussekloo et al. 2017), but it also  
90 has great potential in the simulation of growth and development of the craniofacial system. It  
91 can be used to predict the calvarial growth and to optimize reconstruction of various forms of  
92 craniosynostosis (Wolanski et al. 2013; Li et al. 2013; Libby et al. 2017). However, FE  
93 models require several input parameters and results produced must be validated using  
94 experimental data generated *in vitro* or *in vivo* (e.g. Kupczik et al. 2007; Szwedowski et al.  
95 2011; Toro-Ibacache. et al. 2016). To best of our knowledge, there have not been any  
96 detailed simulations of skull growth (normal or craniosynostotic), which could lead to  
97 improvements in patient management or improvement of craniofacial surgery.

98 This study tests the hypothesis that brain expansion during postnatal development drives  
99 calvarial growth and the response of the calvarial bone and sutures govern the resulting skull  
100 shape. We tested this hypothesis in a FE study to simulate calvarial growth, specific aims  
101 were to: (1) quantify the postnatal calvarial growth in WT and MT mice at P3, 10 and 20; (2)  
102 to develop a FE model of mouse calvarial growth; and (3) to validate the FE predictions by  
103 comparing them to *ex vivo* measurements of the calvaria in WT and MT mouse models.

104

## 105 **2- Materials and Methods**

106 Micro-computed tomography (microCT) images were obtained from wild type and mutant,  
107 *Fgfr2*<sup>C342Y/+</sup>, mice. A series of morphological studies were carried out to quantify the calvarial  
108 growth at P3, P10 and P20. The microCT data of a single P3 mouse were then used to  
109 develop a finite element model to simulate skull growth and in particular to predict mean  
110 calvarial shape at P10. P10 was chosen since 70% of skull growth has been completed at  
111 this stage, with the P20 data included to confirm this (see also Chuang et al., 2011; Moazen  
112 et al., 2016). Several modelling sensitivity tests were performed with the results compared to  
113 a mean specimen identified from the morphological study. This FE model was then used in  
114 the same way but with specified premature fusion of the presphenoid-basisphenoid  
115 synchondrosis (PBS), frontal, coronal, and lambdoid sutures to simulate growth to the  
116 equivalent P10 (MT) mutant geometry.

### 117 **2-1 Morphological analysis**

118 MicroCT scans of a total of 22 WT and MT mice at P3 (n=1 for WT and MT), P10 (n=5 for  
119 WT and MT), and P20 (n=5 for WT and MT), were obtained using an X-Tek HMX160  
120 microCT scanner (XTek Systems Ltd, Hertfordshire, UK). The images had a voxel size of  
121 0.02mm in all directions. Avizo image processing software (FEI Visualization Sciences  
122 Group, Merignac Cedex, France) was used to reconstruct these data into three dimensional  
123 models. The models were positioned so that in the mid-sagittal and transverse planes the  
124 basisphenoid and presphenoid bones were aligned with the horizontal axis. Following this  
125 alignment, calvarial length was measured in the mid-sagittal plane as the distance between  
126 the most anterior part of the frontal suture and the most posterior part of the calvaria (Fig 1).  
127 Calvarial height was measured in the mid-sagittal plane as the distance between the  
128 basisphenoid and the most superior part of the calvaria. Finally, calvarial width was  
129 measured in the transverse plane as the distance between the two most lateral points of the  
130 calvaria. An average specimen at each age and in each group was identified based on the  
131 specimen with the closest length, width and height to the mean values.

132

### 133 **2-2 Finite element analysis**

134 **Model development:** A three dimensional model of the P3 WT mouse was developed from  
135 the microCT data (Fig 2), with bone and sutures segmented and reconstructed in Avizo. The  
136 intracranial volume was defined by filling the whole intracranial volume, hence it was  
137 necessary to ensure that the skull was fully enclosed. Thus the foramen magnum was filled  
138 and areas of the calvaria that were not fully developed were also defined manually. The  
139 model eventually consisted of twenty-three different sections. A surface model of the skull  
140 was then transformed into a meshed solid geometry using Avizo and was then imported into  
141 a finite element software ANSYS v.14.5 (ANSYS Inc., Canonsburg, PA, USA). The model  
142 was meshed using SOLID187 tetrahedral elements (10 node elements with quadratic  
143 displacement behaviours) that are well suited for modelling irregular geometries (ANSYS  
144 Theoretical Manual, v. 14.5). Mesh convergence was carried out, with the final model  
145 defined by over 144,000 elements.

146

147 **Material properties:** All regions were assigned isotropic material properties. In the baseline  
148 model, an elastic modulus of 3500 MPa was assumed for the bone. This was based on  
149 extrapolation of the frontal and parietal bone properties measured in mice at P10, P20, and

150 P70 (Moazen et al. 2015). Sutures and undeveloped areas of bone were assigned an elastic  
 151 modulus of 30 MPa (Henderson et al. 2005; Moazen et al. 2015) while brain (the intracranial  
 152 volume) was modelled with an elastic modulus of 150 MPa. A Poisson's ratio of 0.3 was  
 153 used for all the materials, except 0.48 for the brain (Claessens et al. 1997).

154

155 **Boundary condition and loading:** The intracranial volume expansion during calvarial  
 156 enlargement was modelled by expansion of the intracranial volume (Fig 2) by applying a  
 157 thermal expansion to the ICV material in the FE model to increase its volume. Isotropic linear  
 158 expansion was assumed using the following equation:

$$159 \quad \Delta V = V_1 \times \alpha \times \Delta T \quad (1)$$

160 where  $\alpha$  is the expansion coefficient,  $\Delta V$  the change in volume, equal to the target volume of  
 161 the next age  $V_2$  minus the current volume  $V_1$ . The change in temperature  $\Delta T$  was set at an  
 162 arbitrary constant value of 100°C, and then  $\alpha$  was altered by to achieve the desired ICV  
 163 volume. A thermal expansion that finally led to less than 5% difference between the  
 164 predicted brain and actual brain volume was considered acceptable. Thus, the P3 calvarium  
 165 was initially expanded to the intracranial volume of the wild type P10 (Chuang et al. 2011).  
 166 All degrees of freedom were constrained at three nodes on the presphenoid bone. The  
 167 presphenoid bone was constrained since quantification of the wild type mouse skull growth  
 168 revealed that this bone grows centrally during development and can be considered to  
 169 effectively remain at the same position in the skull.

170

171 **Measurements:** Twenty landmarks (LMs) were used to quantify any differences between  
 172 the predicted P10 skull (from the FE model) and the *ex-vivo* P10 (based on a 3D  
 173 reconstruction from the CT data). While more LMs might have increased the sensitivity of the  
 174 measurements, it was challenging to reliably identify more positions in the P3 geometry due  
 175 to large areas of soft tissue. See Fig. 2 for the LMs details.

176 Root mean square (RMS) differences between the position of the actual and predicted LMs  
 177 were then calculated by the following equation:

178

$$179 \quad RMS = \sqrt{(\sum_{i=1}^n d_i^2) / n}, \quad (2)$$

180

181 where,  $n$  is the number of landmarks and  $d_i$  is the distance between two corresponding  
 182 landmarks of *ex vivo* P10 (in Avizo) and simulated P10 (expanded P3 geometry in ANSYS),  
 183 with  $d_i$  obtained by:

184

$$185 \quad d = \sqrt{(x_2 - x_1)^2 + (y_2 - y_1)^2 + (z_2 - z_1)^2}. \quad (3)$$

186

187 It should be highlighted again that this study is focused on calvarial growth and not facial  
 188 growth, hence no LMs were assigned to the facial bones and an RMS of zero would have  
 189 meant an identical match between the predicted shape and *ex-vivo* results.

190 To quantify the change in the overall shape and to visualise the differences between the  
 191 skulls, 3D distance plots were also created using Avizo. The models were aligned and the  
 192 points on the expanded FE surface mesh were measured to the closest point on the average  
 193 *ex vivo* skull at P10. The areas at which the two surfaces differed (both positively or  
 194 negatively) showed where the FE models over or under-predicted skull growth. The  
 195 maximum differences in both the positive and negative directions were calculated and  
 196 plotted on a colour contour plot.

197

198 **Sensitivity tests:** Three sensitivity tests were carried out on the WT model to investigate the  
199 sensitivity of the results to some of the key input parameters. In particular: (1) boundary  
200 condition: the baseline model in this study was constrained at the presphenoid bone this was  
201 altered to basisphenoid (set 1 in Fig 7A) or both presphenoid and basisphenoid (set 3, Fig.  
202 7A); (2) brain properties: there is a large range of data reported in the literature for brain  
203 properties (e.g. Miller et al. 2000; Gefen & Margulies 2004; Bouchonville et al. 2016) hence  
204 the baseline value of 150MPa was altered within the range from 1MPa to 1500MPa (Fig.  
205 7B); (3) suture properties: our previous experimental measurements (Moazen et al. 2015)  
206 showed a large standard deviation for the suture properties hence the baseline values of  
207 30MPa was varied between 3MPa and 300MPa (Fig. 7C).

208 **Predicting mutant *Fgfr2*<sup>C342Y/+</sup> mouse calvarial shape at P10:** The baseline wild type  
209 model was used to predict the mutant skull shape at P10 after fusion of some of the sutures.  
210 Lui et al. (2013) showed that in this mouse model, several sutures including the  
211 presphenoid-basisphenoid synchondrosis (PBS), frontal, coronal, and lambdoid sutures fuse  
212 prematurely. Hence, they were effectively fused in the wild type model described above by  
213 changing their elastic modulus from suture material to that of bone (3500 GPa). The ICV was  
214 expanded in the same as the WT models and the results were compared against the  
215 microCT data of the MT mice at P10.

216

## 217 Results

### 218 Morphological analysis:

219 Fig 3 summarises the calvarial length, width and height measurements at P3, P10 and P20  
220 for the WT and MT models. While all measurements gradually increased from P3 to P20,  
221 calvarial length and height of the WT mice were consistently higher and lower than the MT  
222 mice respectively. This pattern is also evident in the 2D sagittal cross-sections of the WT  
223 and MT mice (Fig 4).

224 Fig 5 compares the overall morphological differences between the WT and MT mice at P10  
225 using 3D distance colour plots. In the dorsal view, the highlighted square shows the over  
226 growth of the MT skull across the parietal region (bulging). In the posterior view, the  
227 highlighted oval shows the under growth of the lambdoid region in the MT model (Fig 5).

### 228 Finite element analysis:

229 **Sensitivity tests:** Altering the boundary conditions from the baseline model i.e. at the  
230 presphenoid bone (set 2 in Fig 6A) to both basisphenoid (set 1 in Fig 6) and presphenoid  
231 and basisphenoid (set 3, Fig. 6A) leads to overestimation of calvarial height. This was while  
232 the RMS values were decreased from the baseline value of 1.14 to 1.01 and 0.96, for set 1  
233 and 3 respectively. Altering the elastic modulus of the brain had the greatest impact on the  
234 overall skull shape (Fig 6B). Reducing the elastic modulus of the brain led to an increase in  
235 the skull height and bulging of the fronto-parietal region. However, increasing the elastic  
236 modulus of the brain from 15 MPa to 150MPa and 1500MPa led to a closer match with the  
237 overall skull shape of the ex-vivo data and reduced the RMS values from 1.28 to 0.95 for an  
238 elastic modulus change of 15 to 1500 MPa. Increasing the elastic modulus of the sutures  
239 from 3MPa to 300MPa led to a gradual increase in skull height and RMS values from 1.18 to  
240 0.99 (Fig 6C).

241

242 **Predicted WT and MT calvarial shape at P10:** Figure 7 compares the overall geometric  
243 differences (in 2D and 3D) between the FE prediction of skull shape at P10 versus the ex  
244 vivo P10 skull using on the baseline model parameters. The FE model overestimates the  
245 skull height by 0.56mm (highlighted square in Fig 7, 7.19mm vs. 6.63mm) and  
246 underestimates the skull length by 0.21 mm (highlighted oval in Fig 7, 12.93mm vs.  
247 13.14mm). In contrast, using the same parameters, the FE model simulating the MT mice

248 skull shape also overestimates the skull height by 0.16mm (Fig 8, 7.32mm vs. 7.16mm) and  
249 underestimates the skull length by 0.13mm (Fig 8, 12.72mm vs. 12.59mm).

250

251

252

253 **Discussion:**

254 Calvarial growth is thought to involve a series of complex biological, chemical and perhaps  
255 mechanical signalling between a number of soft and hard tissues such as the growing brain,  
256 dura mater, sutures and bone (Morriss-Kay & Wilkie, 2005; Richtsmeier & Flaherty, 2013; Al-  
257 Rekabi et al. in press). This study aims to investigate whether a simple biomechanical  
258 approach simulating expansion of the brain can predict calvarial growth in wild type and a  
259 mouse model of craniosynostosis. The study focuses on prediction of calvarial growth up to  
260 P10, using FE methodology, which corresponds to about one year of age in humans, the  
261 point at which there is clinical consensus advocating surgical treatment of craniosynostosis.  
262 To validate the FE results a series of morphological studies on WT and MT mice were  
263 carried out.

264 The morphological studies highlighted: (1) expansion of the calvaria up to P20 in both WT  
265 and MT; (2) centric growth of the cranial base; (3) the MT mice have a shorter skull length  
266 compared to WT mice and display bulging across the parietal region in line with previous  
267 studies (Eswarakumar et al. 2004; Perlyn et al. 2006; Liu et al. 2013; Martinez-Abadias et al.  
268 2013; Peskett et al. 2017); and most importantly (4) they provided the reference data  
269 required for validation of the FE modelling approach.

270

271 Sensitivity analysis to investigate the choice of input parameters is a key step in any FE  
272 study, therefore a series of sensitivity tests were carried out initially to understand their  
273 impact on the results. In the studies performed, the FE results consistently overestimated the  
274 calvarial height and underestimated the calvarial width (Fig 6). The results highlighted that  
275 the brain (or here the intracranial filling material) properties had the highest impact on the  
276 predictions. The elastic modulus of the brain is reported to be in the range of 1-30 kPa  
277 (Bouchonville et al. 2016). This is three to four orders of magnitude lower than the baseline  
278 value of 150MPa used in this study. This may appear un-realistic, nonetheless since it  
279 generally leads to a similar degree of calvarial expansion to the *ex vivo* data it may have  
280 compensated the effect of other tissues not included here. For instance, dura mater was not  
281 modelled explicitly in this study and is expected to have an elastic modulus in the range of 1-  
282 1000 MPa (e.g. van Noort et al. 1981; Mikos et al. 2008). While it is not clear what is the  
283 combined elastic modulus of the intracranial soft tissues, it is likely to be higher than each of  
284 its individual components and it is perhaps covered in the range of properties tested in the  
285 sensitivity tests here.

286

287 Overall, the finite element models predicted the expansion of the WT and MT model skulls  
288 from P3 to P10 reasonably well. However, there were differences between the FE results  
289 and the *ex vivo* measurements at P10 (Fig 7 and Fig 8). The fact that the FE prediction  
290 constantly overestimates the skull height might be due to not modelling the soft tissues that  
291 cover the brain and perhaps constrain it to the base of the skull i.e. dura matter and  
292 tentorium. On the other hand, while we believe that at early stages of postnatal development  
293 perhaps a uniform growth of the brain is not an unrealistic assumption but it is likely that in  
294 mouse from about P10 onward, brain growth deviates from a uniform radial growth in line  
295 with the bone formations at the sutures to exhibit a more posterior growth (see also Fig 4).

296

297 To the best of our knowledge this is the first attempt to predict calvarial growth in WT and  
298 craniosynostotic MT mice using finite element analysis. A similar approach was recently  
299 tested in humans to predict normal calvarial growth up to one year of age, and it also  
300 showed promising results (Libby et al. 2017). Nonetheless, there are a number of limitations

301 with the current approach that can be improved. These include: (1) several anatomical  
302 structures were not explicitly modelled. For example, the dura mater and cerebellar  
303 tentorium will constrain the brain expansion to some degree; (2) bone forms gradually at the  
304 suture, its thickness and elastic modulus increases during the development, coincident with  
305 skull expansion (Richtsmeier & Flaherty, 2013; Moazen et al. 2015&16). It is likely that  
306 addition of these changes to the model described in this study can enhance the presented  
307 prediction and may lead to better matching of the skull height predictions.

308

309 Considering the limitations mentioned above, modelling an expanding brain using our  
310 methodology, seems to predict skull expansion reasonably well. This suggests that brain  
311 growth may be a key factor in the morphogenesis of the calvarial growth. Future studies are  
312 required to address the limitations of the approach, nonetheless this approach may have  
313 applications in improving management of craniosynostosis, for example through optimisation  
314 of the reconstruction methods for the different various forms of the condition. In the longer  
315 term, this could reduce the number of re-operations for children displaying the condition and  
316 enhance their quality of life.

317

318

### 319 **Acknowledgements**

320 This work was supported by the Royal Academy of Engineering (grant no. 10216/119 to  
321 MM). Authors have no conflict of interest to declare.

322

### 323 **Authors' contribution**

324 MM, MJF, CB and EP designed the study, AM performed the study, AM and JL performed  
325 the analysis, AM, MM, MJF, CB and EP wrote the paper. All authors gave final approval for  
326 publication.

327

328

329

330

331

332

333

334

335

336

337

338

339

340

341

342

343 **References:**

344 **Al-Rekabi Z, Cunningham ML, Sniadecki NJ** (in press). Cell mechanics of  
345 craniosynostosis. *ACS Biom Sci Eng*.

346 **Aggarwal M, Zhang J, Miller MI, Sidman RL, Mori S** (2009). Magnetic resonance  
347 imaging and micro-computed tomography combined atlas of developing and adult mouse  
348 brains for stereotaxic surgery. *Neuroscience*. **162**,1339-1350.

349 **Bouchonville N, Meyer M, Gaude C, Gay E, Ratel D, Nicolas A** (2016). AFM mapping  
350 of the elastic properties of brain tissue reveals kPa  $\mu\text{m}^{-1}$  gradients of rigidity. *Soft*  
351 *Matter*. **12**, 6232-6239.

352 **Boulet SL, Rasmussen SA, Honein MA** (2008). A population-based study of  
353 craniosynostosis in metropolitan Atlanta, 1989-2003. *Am J Med Genet A*. **146A**, 984-  
354 991.

355 **Chuang N, Mori S, Yamamoto A, Jiang H, Ye X, Xu X, Richards LJ, Nathans**  
356 **J, Miller MI, Toga AW, Sidman RL, Zhang J** (2011). An MRI-based atlas and database  
357 of the developing mouse brain. *Neuroimage*. **54**, 80-89.

358 **Claessens M, Sauren F, Wismans J** (1997). Modeling of the human head under impact  
359 conditions: a parametric study. *SAE Technical Paper*. 973338.

360 **Cohen MM** (2005). Editorial: perspectives on craniosynostosis. *Am J Med Genet A*.  
361 **136A**, 313-326.

362 **Cornelissen M, Ottelander Bd, Rizopoulos D, van der Hulst R, Mink van der Molen**  
363 **A, van der Horst C, Delye H, van Veelen ML, Bonsel G, Mathijssen I** (2016). Increase  
364 of prevalence of craniosynostosis. *J Cranio-Max-Fac Surg*. **44**,1273-1279.

365 **Cox PG, Rayfield EJ, Fagan MJ, Herrel A, Pataky TC, Jeffery N** (2012). Functional  
366 evolution of the feeding system in rodents. *PLoS One* **7**: e36299.

367 **Curtis N, Jones MEH, Shi J, O'Higgins P, Evans SE, Fagan MJ** (2011). Functional  
368 relationship between skull form and feeding mechanics in *Sphenodon* and implications  
369 for Diapsid skull development. *PLoS ONE* **6(12)**, e29804.

370 **Dekaban AS** (1977). Tables of cranial and orbital measurements, cranial volume, and  
371 derived indexes in males and females from 7 days to 20 years of age. *Ann. Neurol.* **2**,  
372 485-491.

373 **Eswarakumar VP, Horowitz MC, Locklin R, Morriss-Kay GM, Lonai P** (2004). A gain-  
374 of-function mutation of *Fgfr2c* demonstrates the roles of this receptor variant in  
375 osteogenesis. *Proc Natl Acad Sci USA*. **101**,12555-12560.

376 **Gefen A, Margulies SS** (2004). Are in vivo and in situ brain tissues mechanically  
377 similar? *J Biomech*. **37**,1339-1352.

378 **Grova M, Lo DD, Montoro D, Hyun JS, Chung MT, Wan DC, Longaker MT** (2012).  
379 Models of cranial suture biology. *J Craniofac Surg*. **23**,1954–1958.

380 **Gussekloo SW, Berthaume MA, Pulaski DR, Westbroek I, Waarsing JH, Heinen R,**  
381 **Grosse IR, Dumont ER** (2017). Functional and evolutionary consequences of cranial  
382 fenestration in birds. *Evolution*. **71**, 1327-1338.

383 **Henderson JH, Chang LY, Song HM, Longaker MT, Carter DR** (2005). Age-  
384 dependent properties and quasi-static strain in the rat sagittal suture. *J Biomech*. **38**,  
385 2294-2301.

386 **Herring SW** (2008). Mechanical influences on suture development and patency. *Front*  
387 *Oral Biol*. **12**, 41-56.

388 **Holmes G** (2012). The role of vertebrate models in understanding craniosynostosis.  
389 *Childs Nerv Syst*. **28**,1471–1481.

390 **Johnson D, Wilkie AOM** (2011). Craniosynostosis. *Eur J Hum Genet*. **19**, 369–376.



- 391 **Kupczik K, Dobson CA, Fagan MJ, Crompton RH, Oxnard CE, O'Higgins P** (2007).  
392 Assessing mechanical function of the zygomatic region in macaques: validation and  
393 sensitivity testing of finite element models. *J Anat.* **210**, 41–53.
- 394 **Li Z, Luo X, Zhang J** (2013). Development/ global validation of a 6-month-old pediatric  
395 head finite element model and application in investigation of drop-induced infant head  
396 injury. *Comput Methods Programs Biomed.* **112**, 309-319.
- 397 **Libby J, Marghoub A, Johnson D, Khonsari RH, Fagan MJ, Moazen M** (2017).  
398 Modelling human skull growth: a validated computational model. *J Roy Soc Int.* **14**,  
399 20170202.
- 400 **Liu J, Nam HK, Wang E, Hatch N** (2013). Further analysis of the Crouzon mouse:  
401 effects of the FGFR2(C342Y) mutation are cranial bone-dependent. *Calcif Tissue Int.* **92**,  
402 451-466.
- 403 **Martínez-Abadías N, Motch SM, Pankratz TL, Wang Y, Aldridge K, Jabs EW,**  
404 **Richtsmeier JT** (2013). Tissue-specific responses to aberrant FGF signaling in complex  
405 head phenotypes. *Dev Dyn.* **242**, 80-94.
- 406 **Maikos JT, Elias RA, Shreiber DI** (2008). Mechanical properties of dura mater from the  
407 rat brain and spinal cord. *J Neurotrauma.* **25**, 38-51.
- 408 **Miller K, Chinzei K, Orssengo G, Bednarz P** (2000). Mechanical properties of brain  
409 tissue in-vivo: experiment and computer simulation. *J Biomech.* **33**, 1369-1376.
- 410 **Moazen M, Alazmani A, Rafferty K, Liu ZJ, Gustafson J, Cunningham ML, Fagan**  
411 **MJ, Herring SW** (2016). Intracranial pressure changes during mouse development. *J.*  
412 *Biomech.* **49**, 123-126.
- 413 **Moazen M, Costantini D, Bruner E** (2013). A sensitivity analysis to the role of fronto-  
414 parietal suture in *Lacerta bilineata*: a preliminary finite element approach. *Anat Rec.*  
415 **296**, 198-209.
- 416 **Moazen M, Peskett E, Babbs C, Pauws E, Fagan MJ** (2015). Mechanical properties of  
417 calvarial bones in a mouse model for craniosynostosis. *PLoS ONE.* **10**, e0125757.
- 418 **Mooney MP, Siegel MI, Burrows AM, Smith TD, Losken HW, Dechant J, Cooper G,**  
419 **Kapucu MR** (1998). A rabbit model of human familial, nonsyndromic, unicoronal suture  
420 synostosis: part 1. Synostotic onset, pathology, and sutural growth patterns. *Childs Nerv*  
421 *Syst.* **14**, 236-246.
- 422 **Morriss-Kay GM, Wilkie AOM** (2005). Growth of the normal skull vault and its alteration  
423 in craniosynostosis: insights from human genetics and experimental studies. *J Anat.* **207**,  
424 637-653.
- 425 **Opperman LA** (2000). Cranial Sutures as intramembranous bone growth sites. *Dev*  
426 *Dyn.* **485**, 472-485.
- 427 **Perlyn CA, DeLeon VB, Babbs C, Govier D, Burell L, Darvann T, Kreiborg S,**  
428 **Morriss-Kay G** (2006). The craniofacial phenotype of the Crouzon mouse: analysis of a  
429 model for syndromic craniosynostosis using three-dimensional MicroCT. *Cleft Palate J.*  
430 **43**, 740-748.
- 431 **Peskett E, Kumar S, Baird W, Jaiswal J, Li M, Patel P, Britto JA, Pauws E** (2017).  
432 Analysis of the Fgfr2<sup>C342Y</sup> mouse model shows condensation defects due to  
433 misregulation of Sox9 expression in prechondrocytic mesenchyme. *Biol Open.* **6**, 223-  
434 231.
- 435 **Rayfield EJ** (2007). Finite element analysis and understanding the biomechanics and  
436 evolution of living and fossil organisms. *Annu Rev Earth Planet Sci.* **35**, 541–576.
- 437 **Ross CF, Patel BA, Slice DE, Strait DS, Dechow PC, Richmond BG, Spencer MA**  
438 (2005). Modeling masticatory muscle force in finite element analysis: sensitivity analysis  
439 using principal coordinates analysis. *Anat Rec.* **283A**, 288–299.
- 440 **Richtsmeier JT, Flaherty K** (2013). Hand in glove: brain and skull in development and  
441 dysmorphogenesis. *Acta Neuropathol.* **125**, 469-489.
- 442 **Sperber GH** (1989). Craniofacial embryology, 4<sup>th</sup> edition, p. 102. London: Wright,  
443 Butterworths.

444 **Szwedowski TD, Fialkov J, Whyne CM** (2011). Sensitivity analysis of a validated  
445 subject-specific finite element model of the human craniofacial skeleton. *Proc Inst Mech*  
446 *Eng H.* **225**, 58-67.

447 **Toro-Ibacache V, Fitton LC, Fagan MJ, O'Higgins P** (2016). Validity and sensitivity of  
448 a human cranial finite element model: implications for comparative studies of biting  
449 performance. *J Anat.* **228**, 70-84.

450 **van der Meulen J, van der Hulst R, van Adrichem L, Arnaud E, Chin-Shong D,**  
451 **Duncan C, Habets E, Hinojosa J, Mathijssen I, May P, et al.** (2009). The increase of  
452 metopic synostosis a pan-european observation. *J Craniofac Surg.* **20**, 283-286.

453 **van Noort R, Black MM, Martin TR, Meanley S** (1981). A study of the uniaxial  
454 mechanical properties of human dura mater preserved in glycerol. *Biomaterials.* **2**, 41-5.

455 **Wilkie AOM** (1997). Craniosynostosis: genes and mechanisms. *Hum Mol Genet.* **6**,  
456 1647-1656.

457 **Wolanski W, Larysz D, Gzik M, Kawlewska E** (2013). Modeling and biomechanical  
458 analysis of craniosynostosis correction with the use of finite element method. *Int J*  
459 *Numerl Method Biomed Eng.* **29**, 916-925.

460

461

462

463

464

465

466

467

468

469

470

471

472

473

474

475

476

477

478

479

480

481

482 **Figure captions:**

483 Fig 1: Lateral and dorsal view of a P3 mouse skull, highlighting landmark positions, length,  
484 height and width measurement. Note: 1& 2 Most medial intersection of the frontal and  
485 parietal bones, on the frontal (left & right); 3&4 Most medial intersection of the frontal and  
486 parietal bones, on the parietal (left and right); 5&6 Most lateral intersection of the frontal and  
487 parietal bones, on the frontal (left and right); 7&8 Midpoint on medial side of the parietal  
488 bone (left & right); 9&10 Most posterior-inferior point on the parietal (left and right); 11 &12  
489 Intersection of the squamosal to the zygomatic process of squamous portion of temporal  
490 bone (left & right); 13&14 Most posterior-inferior point on the interparietal (left & right); 15  
491 Most anterior-medial point of the interparietal bone; 16 Most anterior-medial point of the  
492 occipital bone; 17&18 Most posterior-lateral point of the occipital bone; 19 Most posterior-  
493 medial point of the occipital bone; 20 Most posterior-medial point of the basioccipital bone.

494 Fig 2: Finite element model development and loading.

495 Fig 3: Length, width and height measurement at P3, P10 and P20.

496 Fig 4: Sagittal cross section of *ex vivo* wild type (WT) and mutant type (MT) mice at P3, P10  
497 and P20.

498 Fig 5: 3D morphological comparison between the P10 wild type (WT) and mutant type (MT)  
499 mice.

500 Fig 6: Sensitivity analysis to the choice of (A) boundary condition, (B) elastic modulus of the  
501 brain, and (C) sutures. Dashed outlines highlight the baseline values and results.

502 Fig 7: 3D morphological comparison between the finite element (FE) predicted and *ex vivo*  
503 wild type (WT) mouse at P10.

504 Fig 8: 3D morphological comparison between the finite element (FE) predicted and *ex vivo*  
505 mutant type (MT) mouse at P10.

506

507

508

509

510

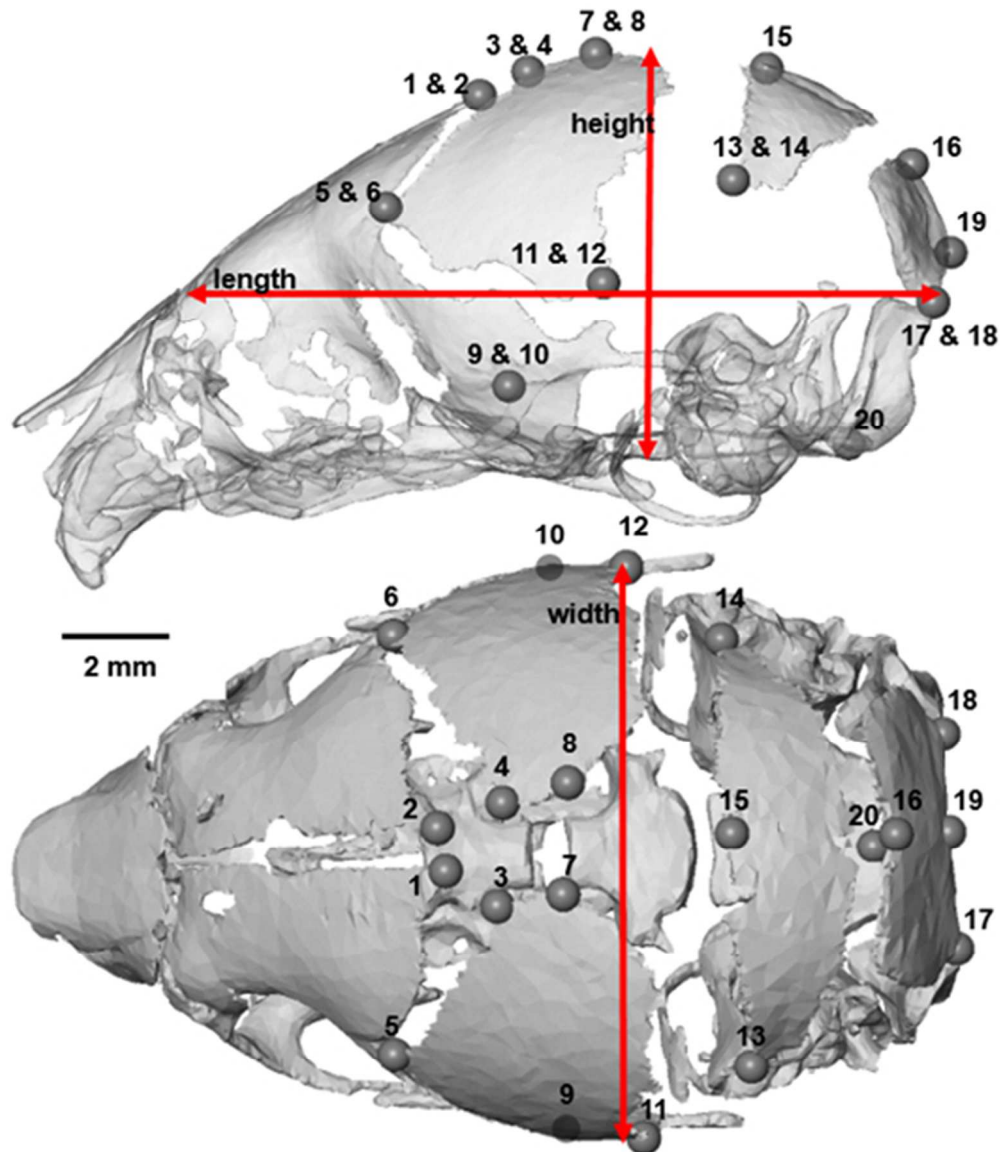


Fig 1: Lateral and dorsal view of a P3 mouse skull, highlighting landmark positions, length, height and width measurement. Note: 1& 2 Most medial intersection of the frontal and parietal bones, on the frontal (left & right); 3&4 Most medial intersection of the frontal and parietal bones, on the parietal (left and right); 5&6 Most lateral intersection of the frontal and parietal bones, on the frontal (left and right); 7&8 Midpoint on medial side of the parietal bone (left & right); 9&10 Most posterior-inferior point on the parietal (left and right); 11 &12 Intersection of the squamosal to the zygomatic process of squamous portion of temporal bone (left & right); 13&14 Most posterior-inferior point on the interparietal (left & right); 15 Most anterior-medial point of the interparietal bone; 16 Most anterior-medial point of the occipital bone; 17&18 Most posterior-lateral point of the occipital bone; 19 Most posterior-medial point of the occipital bone; 20 Most posterior-medial point of the basioccipital bone.

70x81mm (192 x 192 DPI)

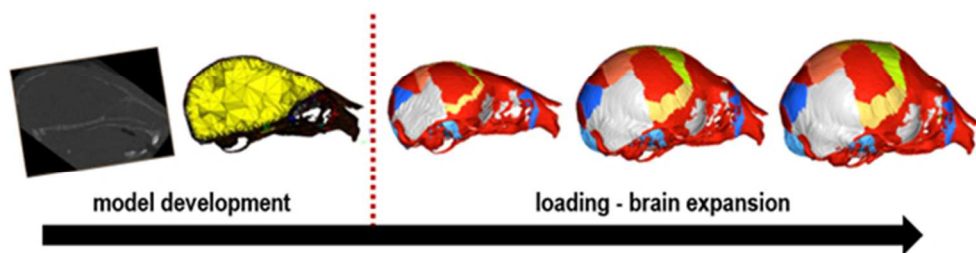


Fig 2: Finite element model development and loading.

79x22mm (192 x 192 DPI)

Peer Review Only

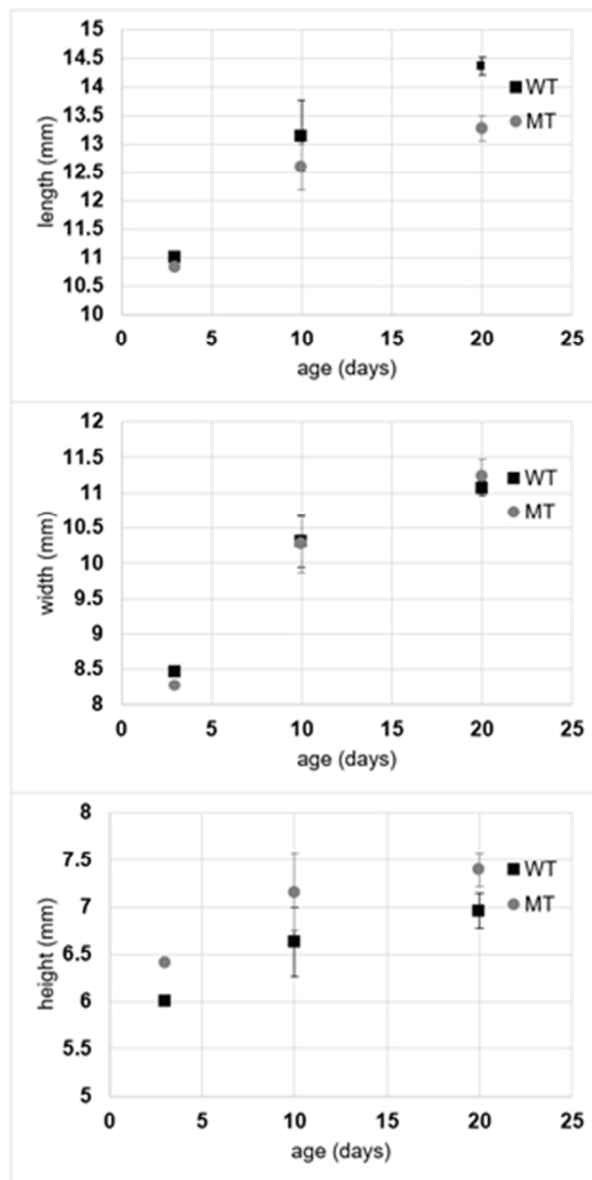


Fig 3: Length, width and height measurement at P3, P10 and P20.

43x83mm (192 x 192 DPI)

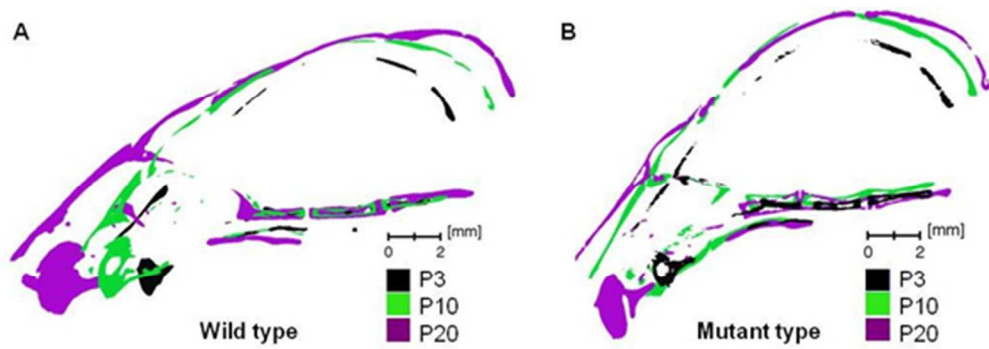


Fig 4: Sagittal cross section of ex vivo wild type (WT) and mutant type (MT) mice at P3, P10 and P20.

78x28mm (192 x 192 DPI)

Peer Review Only

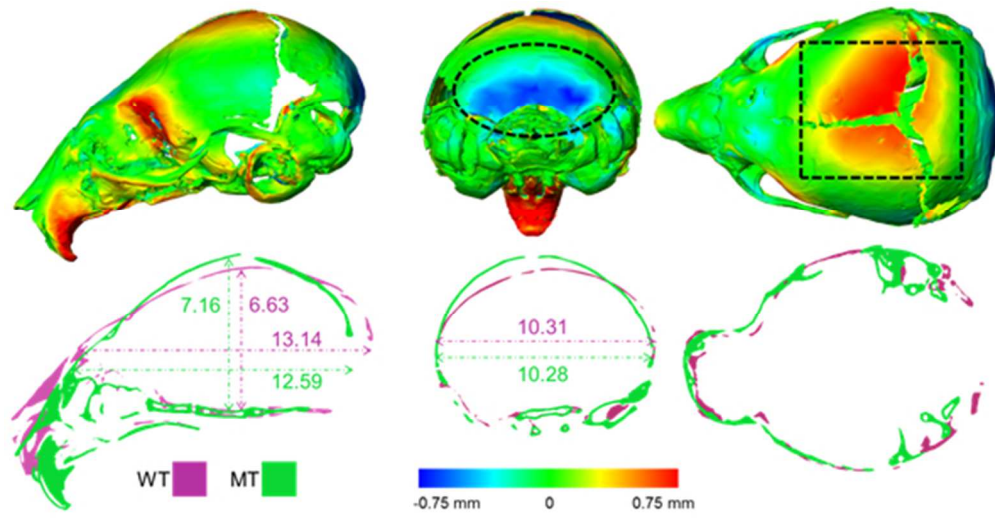


Fig 5: 3D morphological comparison between the P10 wild type (WT) and mutant type (MT) mice.

78x40mm (192 x 192 DPI)

Review Only



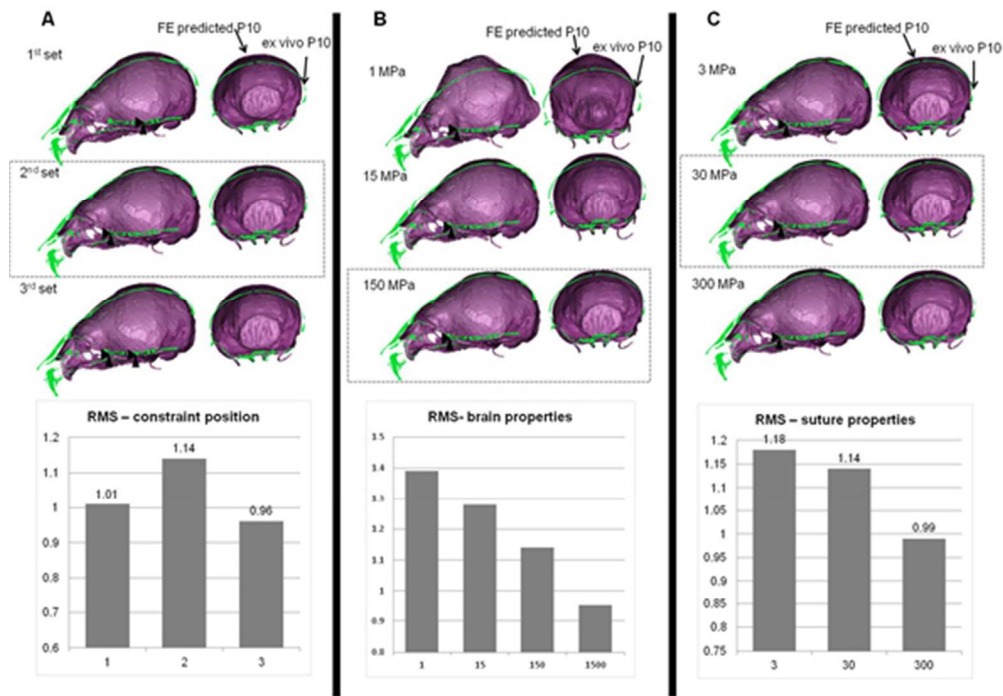


Fig 6: Sensitivity analysis to the choice of (A) boundary condition, (B) elastic modulus of the brain, and (C) sutures. Dashed outlines highlight the baseline values and results.

78x54mm (192 x 192 DPI)

View Only

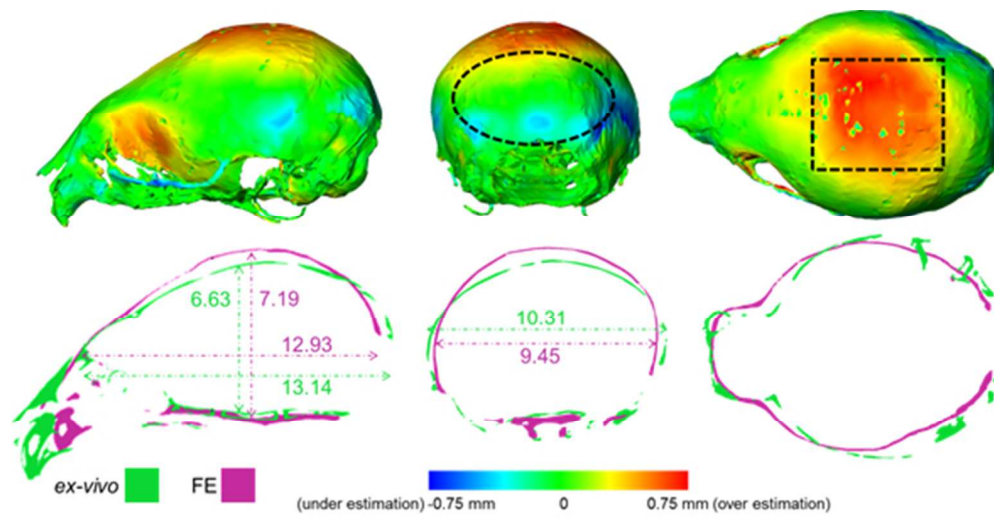


Fig 7: 3D morphological comparison between the finite element (FE) predicted and ex vivo wild type (WT) mouse at P10.

78x40mm (192 x 192 DPI)

Review Only

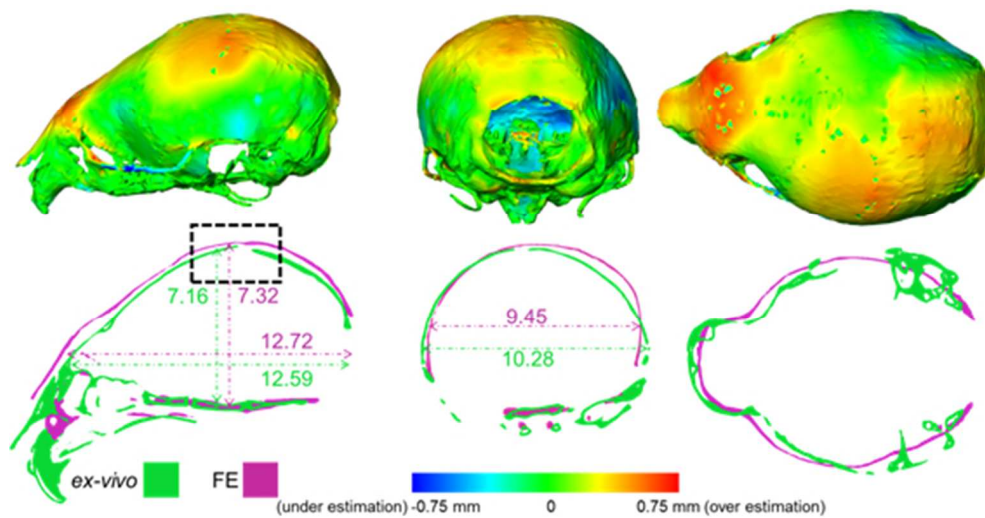


Fig 8: 3D morphological comparison between the finite element (FE) predicted and ex vivo mutant type (MT) mouse at P10.

76x39mm (192 x 192 DPI)